Systematic study of exciton diffusion length in organic semiconductors by six experimental methods

By Jason Lin, Oleksandr V. Mikhnenko, Jingrun Chen, Zarifi Masri, Arvydas Ruseckas, Alexander Mikhailovsky, Reilly Raab, Jianhua Liu, Paul W. M. Blom, Maria Antonietta Loi, Carlos J. Garcia-Cervera, Ifor D.W. Samuel and Thuc-Quyen Nguyen

Received (in XXX, XXX) Xth XXXXXXXXX 20XX, Accepted Xth XXXXXXXXX 20XX
DOI: 10.1039/b000000x

SUPPLEMENTARY INFORMATION

1. Steady-state and Time-resolved Photoluminescence Surface Quenching

Steady-state photoluminescence (PL) surface quenching (SS-SQ) and time-resolved PL surface quenching (TR-SQ) are two techniques which have been often employed to measure exciton diffusion length.[1–11] In surface quenching techniques, bi-layers are prepared of an organic semiconductor and an exciton quenching layer. Samples are excited with a laser and PL intensity or PL decay time is detected. Then the PL of bi-layers is compared with thin films that do not have the quenching layer. The PL of bi-layers appears to be much weaker with shorter decay time if the thickness of organic semiconductor is of the order of the exciton diffusion length. By modelling PL quenching efficiency one extracts the exciton diffusion length and diffusion coefficient. Surface quenching techniques are advantageous because the exciton diffusion length is measured directly.

Due to a large number of assumptions and requirements with surface quenching techniques, it is difficult to accurately use these methods on practice. Thin film morphology must be consistent across the thickness range of typically 5-50 nm. This is likely not the case for crystalline and semi crystalline materials. As discussed in Section 7, spectroscopic ellipsometry measurements on films of A, B, and C of varying thicknesses showed that all films are predominantly isotropic. Where therefore expect the morphology of films A, B, and C to be consistent across the thicknesses explored in this work. Surface quenching techniques also require a sharp interface between the organic semiconductor and exciton quencher layers. The surface roughness of both layers must be less than 1 nm on the area of 100 μm^2. And finally, the excitons quenching efficiency must be known at interfaces with exciton quenching layer, vacuum, and with substrate (usually quartz).

A common challenge when employing the SS-SQ and TR-SQ techniques is finding a quencher that has a high quenching efficiency and the ability to form a sharp bilayer interface with the organic semiconductor. In this study, the choice of quencher was chosen by measuring the TR PL on bilayers films consisting of a thin (~ 5 nm) layer of compound B with TiO_2,[5] [6,6]-Phenyl C61 butyric acid (PCBA) modified TiO_2, N719 ruthenium dye modified TiO_2,[5] poly(benzimidazobenzophenanthroline ladder) (BBL),[12–15] or evaporated C_{60} (Fig. S1). Of the quenchers tested, evaporated C_{60} quenched the PL of compound B the greatest. As a result, the SS-SQ and TR-SQ techniques were performed using a 4 nm evaporated C_{60} layer to serve as the quencher. It should be noted that we cannot rule out the possibility of C_{60} diffusion into the organic semiconductor layer. Inter-diffusion would enhance the quenching efficiency and lead to an overestimation of the exciton diffusion length. However, in this work we observed similar diffusion coefficients and diffusion lengths for surface and bulk quenching techniques (Table 2).

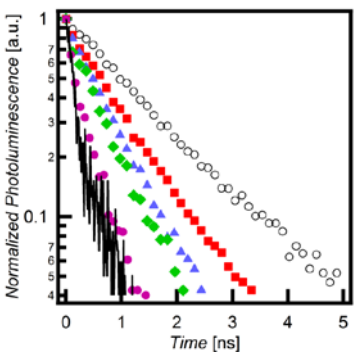

Fig. S1 Time resolved PL of a thin (~ 5 nm) layer of B with a quenching layer of TiO_2 (red square), PCBA modified TiO_2 (blue triangle), N719 modified TiO_2 (green diamond), BBL (purple circle), or C_{60} (black line). Time resolved PL was also measured on a thin (~ 5 nm) layer of B without a quencher (open circle) for reference.

In regards to the fabrication procedure, microscope slides (Corning Inc.) with 1 mm thicknesses were cut into 40 × 40 mm squares. The surface root mean squared (RMS) roughness was measured at 1 nm with atomic force microscopy. All glass slides were manually

scrubbed with unscented liquid dish soap (Ivory) and sonicated (Fisher Scientific) in a series of deionized water, acetone, and isopropanol (VWR International) for 15 minutes each. Slides were then dried under nitrogen stream and stored overnight in a 90 °C laboratory oven. All organic semiconductor materials were synthesized in-house as previously reported.[16] All solutions and film preparation were done in a nitrogen filled glove box. Solutions were prepared at 14 mg/mL with anhydrous chloroform (Sigma Aldrich). Solutions were left to stir overnight at 60 °C.

Solutions were spun onto the cleaned microscope slides with a deposition volume of 100 µL, spin rate of 1500 rpm, and a spin time of 60 seconds. The film thickness was varied by subsequently diluting the stock solution followed by spin casting. This procedure was repeated in order to obtain concentrations ranging from 14 mg/mL to 1 mg/mL. We used shadow mask to evaporate C_{60} on only half of the substrate. The samples were transferred into an evaporation chamber inside a glovebox, which was subsequently evacuated to 10^{-7} torr (Angstrom Engineering). Approximately 4 nm of C_{60} (Fisher Scientific) was thermally evaporated onto the samples at a rate of 0.1 Å per second.

To protect the films from ambient conditions the samples were encapsulated inside the nitrogen glovebox. A Teflon tweezer was used to scrape the previously deposited materials off of the glass in a band ~2-4 mm of from the edges of the glass, providing a bare glass perimeter around the center of the sample to which a two-part epoxy (Kimball Midwest) was then applied. A second 40 × 40 mm bare glass slide was placed on top of the epoxy and left to cure for two hours. Scraping off the organic layer with a Teflon tweezer strengthens the encapsulation thereby preventing delamination and oxygen diffusion into the encapsulated films. After the epoxy cured, the samples were removed from the glovebox for measurements. The finalized films had a film structure of glass/organic semiconductor/nitrogen/glass. The procedure above was repeated for 10 different thicknesses of the organic semiconductor with and without a quenching layer.

Steady-state PL measurements were performed using an Ar^+-laser (Spectraphysics Beamlok 2060) tuned to 457 nm wavelength. The excitation laser beam was incident normal to the glass substrate used for deposition of the organic layers. PL was collected normal from glass substrate used for encapsulation on the opposite side of the sample. An interference long wavelength-pass filter (Omega Filters) was used to block the excitation light. The PL was focused on the entrance slit of a monochromator (Acton SP-500) by a system of lenses. The spectra were recorded using spectroscopic charge-coupled device (CCD) camera (Princeton Instruments PIXIS:400). PL life-time measurements were performed using Time-Correlated Single Photon Counting (TCSPC) technique.[17] Approximately 200 femtosecond (fs) excitation pulses with wavelength 400 nm were generated by doubling the fundamental frequency of fs Ti:Sapphire laser (Coherent Mira 900) pulses in a commercial optical harmonic generator (Inrad). The laser repetition rate was reduced to 2 MHz by a home-made acousto-optical pulse picker in order to avoid saturation of the chromophore. TCSPC system is equipped with an ultrafast microchannel plate photomultiplier tube detector (Hamamatsu R3809U-51) and electronics board (Becker & Hickl SPC-630) and has instrument response time about 60-65 picoseconds. Triggering signal for the TCSPC board was generated by sending a small fraction of the laser beam onto a fast (400 MHz bandwidth) Si photodiode (Thorlabs Inc.). The pulsed laser beam was aligned collinearly with the CW laser beam and the same optical system, laser blocking filter, and monochromator were used for time-resolved and steady-state PL measurements. The mean excitation power for the steady-state and time-resolved PL measurements were measured at 1.6 and 1.1 W/cm^2, respectively. When applying the SS-SQ technique it is assumed that the absorption from the quenching layer is negligible. For this reason is preferable to use very thin layers of C_{60} or TiO_2.

Upon completion of PL measurements all films were pried open with a razor blade. Exposed films were then characterized with spectroscopic ellipsometry (J.A. Woollam Co., Inc.) to yield the film thickness and optical constants of all the layers (see Section 2). The exposed films were also characterized with tapping mode atomic force microscopy (Innova) to yield the RMS roughness. All films in this study have RMS roughness values around 1 nm. Thicknesses were also measured with a profilometer (Abios XP-100) which showed good agreement with thicknesses obtained from ellipsometry.

Figure S2 shows the steady-state PL spectrum for bilayers consisting of a 4 nm evaporated C_{60} layer on top of a film of A (Fig. S2a), B (Fig. S2b), and C (Fig. S2c) of varying thicknesses.

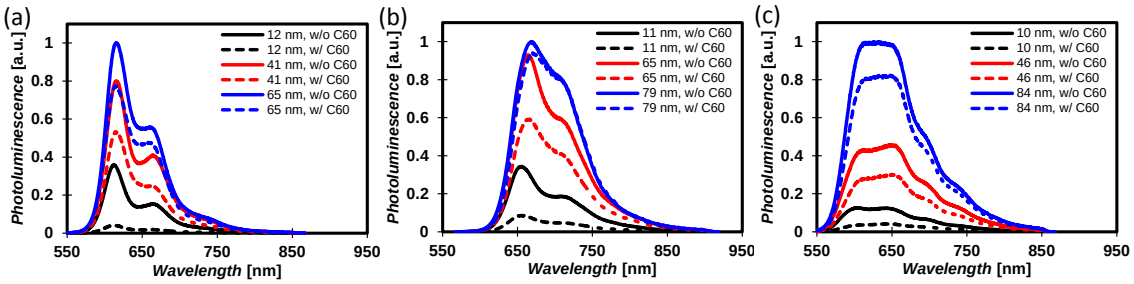

Fig. S2 Steady state PL for (a) A, (b) B, and (c) C films with (dotted lines) and without (solid lines) a C_{60} (4 nm) quenching layer. All spectra were normalized by the maximum value in the thickest control (no C_{60}) film.

For thin film (~ 11 nm) the integrated steady-state PL for bilayers with a C_{60} quenching layer is significantly less than that of the control film without C_{60}. In contrast, for thick films (~ 65 – 85 nm) the integrated steady-state PL for bilayers with and without a C_{60} quenching layer are nearly equivalent. PL spectra were used to calculate the relative quenching efficiencies Q:

$$Q = 1 - \frac{\int PL_{quencher} d\lambda}{\int PL_{pristine} d\lambda}, \quad (1)$$

where $\int PL_{quencher} d\lambda$ and $\int PL_{pristine} d\lambda$ are the integrated PL for the bilayers films with quencher and the pristine films without quencher

respectively. The PL decay was normalized to the value at t = 0 prior to the integration. Figure S3 shows the relative quenching efficiency (filled circles) as a function of film thickness for bilayers of A (Fig. S3a), B (Fig. S3b), and C (Fig. S3c) with C_{60} (4 nm). For thin films, the majority of generated excitons reach the quenching interface which results in a quenching efficiency that approaches unity. In contrast, only a small fraction of the generated excitons reach the quenching interface in thick films which yields a low quenching efficiency.

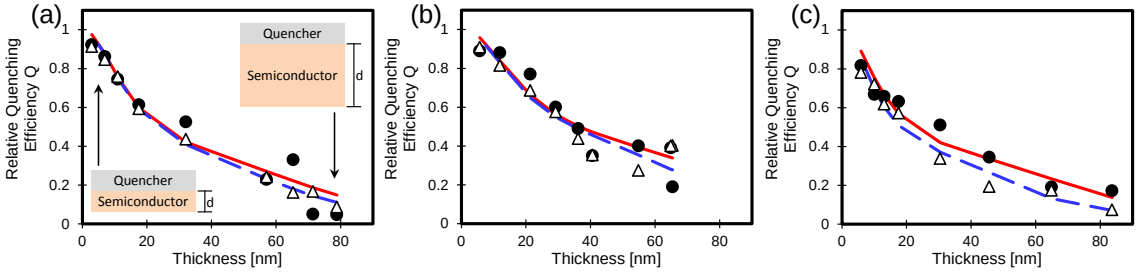

Fig. S3 Relative quenching efficiency obtained from steady-state (filled circles) and time-resolved (open triangles) PL quenching measurements on bilayer films of (a) A, (b) B, and (c) C with a 4 nm C_{60} layer. A transfer matrix model was used to simulate the relative quenching efficiency for the steady-state (solid red line) and time-resolved (dashed blue line) measurements.

An alternative to using steady-state PL as in the SS-SQ technique is to measure with time-resolved PL as in the TR-SQ technique. Figure S4 shows the time-resolved PL for bilayers of A (Fig. S4a), B (Fig. S4b), and C (Fig. S4c) with C_{60} (4 nm). It is important to note that the SS-SQ and TR-SQ techniques can be performed on the same set of fabricated bilayer films as was done in this work. The PL decay curves in Figure S4 show that the decay rate is accelerated as the film thickness is decreased. Fitted lifetimes for the pristine films measured in UCSB, St Andrews, and Groningen are summarized in Table S1.

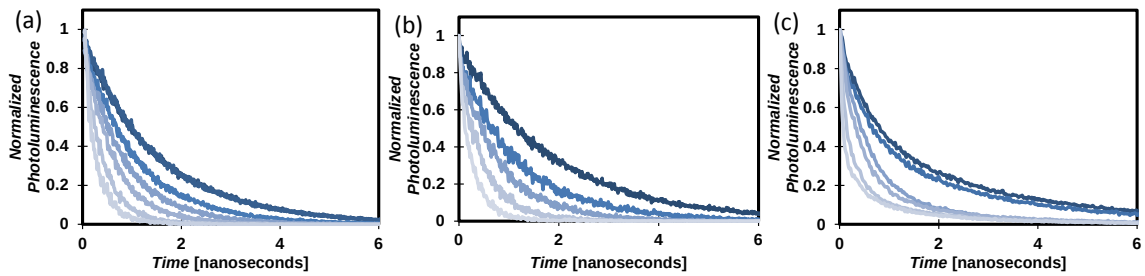

Fig.S4 Time-resolved PL for bilayers of (a) A, (b) B, and (c) C with a C_{60} (4nm) quenching layer for decreasing thickness (dark to lighter curves). All decay curves were normalized by the value at time zero.

Table S1 Exciton lifetime for compounds A, B, and C measured in different laboratories.

Technique	A	B	C
SS-SQ & TR-SQ	1540 ± 20	2150 ± 60	2010 ± 20
EEA	1450 ± 100	1370 ± 20	1620 ± 20
BQ-MC & BQ-SV	1810 ± 60	2240 ± 40	1394 ± 10

* All lifetimes in picoseconds

The PL decay curves are normalized at the peak and integrated to determine the quenching efficiency:

$$Q = 1 - \frac{\int PL_{quencher}\, dt}{\int PL_{pristine}\, dt}, \tag{2}$$

where $\int PL_{quencher} dt$ and $\int PL_{pristine} dt$ are the integrated PL for the bilayer films with and without quencher. Figure S3 shows the relative quenching efficiency (open triangles) as a function of organic semiconductor thickness for bilayers of A (Fig. S3a), B (Fig. S3b), and C (Fig. S3c) with 4 nm C_{60}. As expected, the quenching efficiency is nearly unity for thin films and approaches zero for thick films. In general, we see good agreement in quenching efficiencies between the SS-SQ and TR-SQ techniques. However, the TR-SQ technique is preferred since time-resolved measurements are less sensitive to the orientation of excitation and collection in comparison to steady-state measurements.

To describe the generation, diffusion, and extinction of excitons, we use the following model:

$$\frac{\partial n(x,t)}{\partial t} = D\frac{\partial^2 n(x,t)}{\partial x^2} - \frac{n(x,t)}{\tau} + G(x,t), \tag{3}$$

where $n(x,t)$ is the exciton density at point x and time t, D is the exciton diffusion constant, τ is the exciton lifetime, d is the thickness of the active layer, and $G(x,t)$ is the exciton generation rate. Experimentally the laser is turned on only for a short period, of the order of a 200 picoseconds, while the diffusion process happens in a time scale of the order of nanoseconds and PL happens in even longer time scales, so we can write $G(x,t) = g(x)\delta(t-t_0)$ where δ is a delta-type function. We use the transfer matrix approach[18] to calculate $g(x)$.

Equation 3 must be supplemented with appropriate initial and boundary conditions. We assume that initially there are no excitons in the system, and therefore set $n(x,0) = 0$. When there is no quencher in the system we impose no-flux boundary conditions at both interfaces, i.e., $D\frac{\partial n(0,t)}{\partial x} = 0$ and $D\frac{\partial n(d,t)}{\partial x} = 0$. When a quencher is present on the interface located at $x = d$, we impose $D\frac{\partial n(0,t)}{\partial x} = 0$, and $n(d,t) = 0$. This last condition takes into account the charge transfer effect between the active layer and the quencher. In certain cases it has been shown[5] that energy transfer effect between the active layer and the quencher plays an important role, in which case Equation 3 is modified to

$$\frac{\partial n(x,t)}{\partial t} = D\frac{\partial^2 n(x,t)}{\partial x^2} - \frac{n(x,t)}{\tau} - k_F n(x,t) + G(x,t), \tag{4}$$

where $k_F = \frac{C_A \pi R_0^6}{\tau 6(d-x)^3}$ is the Förster energy transfer term with the energy acceptor molecular density $C_A \sim 1.4/\text{nm}^3$ for C60.[5]

Although Equations 3 and 4 can be solved explicitly in simple cases,[19] this is no longer possible when the Förster term is present. We therefore solve the equations numerically using finite differences. We have considered both equilibrium and time-integrated measurements of PL. For the equilibrium case, we simply set the time derivative equal to zero in Equations 3 and 4, which recovers the equations used for steady-state PL measurements.[19] For the time-integrated case, integrating in time over (0, ∞) in Equations 3 and 4 produces

$$D\frac{d^2 n(x)}{dx^2} - \frac{n(x)}{\tau} + G(x) = n(x,\infty) - n(x,0) = 0 \tag{5}$$

with boundary conditions $-D\frac{dn(x=0)}{dx}$=0 and $D\frac{dn(x=d)}{dx}$=0 , and

$$D\frac{d^2 n(x)}{dx^2} - \frac{n(x)}{\tau} + k_F n(x) + G(x) = 0 \tag{6}$$

with boundary conditions $-D\frac{dn(x=0)}{dx} = 0$ and $n(x=d) = 0$. Here $n(x) = \int_0^\infty n(x,t)dt$ and $G(x) = \int_0^\infty G(x,t)dt$. Note that steady-state equations (5) and (6) are equivalent to time-dependent equations (3) and (4). Therefore, instead of solving equations (3) and (4), we solve equations (5) and (6). In equations (5) and (6), the exciton density is computed by time integration. Experimentally, the number of excitons is counted at each time step and then summed up over all times to produce the exciton density for comparison with equations (5) and (6), instead of equations (3) and (4). In this way, we can ensure the equivalence between the time-dependent study and the steady-state study. This is also verified by how close exciton diffusion lengths of SS-SQ and TR-SQ techniques in Table 2 and Fig2 in Main Text. Using $L_D = \sqrt{D\tau}$, we rewrite Equations 5 and 6 as

$$L_D^2\frac{d^2 n(x)}{dx^2} - n(x) + G(x)\tau = 0 \tag{7}$$

and

$$L_D^2\frac{d^2 n(x)}{dx^2} - n(x) - \frac{C_A \pi R_0^6}{6(d-x)^3}n(x) + G(x)\tau = 0 \tag{8}$$

respectively.

The PL is then measured by $PL(d) = \int_0^d n(x)\varepsilon(x)dx$, where $\varepsilon(x)$ is the light extraction efficiency and is assumed to be a constant here. Denote PL of quenching and nonquenching cases by $PL_q(d)$ and $PL_n(d)$, respectively. The diffusion length L_D is then obtained by solving the following least-squares approximation:

$$\min_{L_D} \frac{1}{N}\sum_{i=1}^{N}\left(\frac{PL_q(d_i)}{PL_n(d_i)} - R(d_i)\right)^2, \tag{9}$$

where N is the number of samples, and $R(d)$ is the ratio between PL of quenching and nonquenching cases measured in experiments. We solve the optimization problem (9) using Newton's method with a linesearch technique.[20] We use second order finite differences to solve Equations 7 and 8 with grid size $h = 0.1$ nm. Note that a rescaling of the generation term $G(x)$ in Equation 5 by a constant results in a rescaling of $n(x)$ by the same factor. This factor cancels out in the ratio of PL in Equation 9, which explains why the lifetime τ does not appear in Equation 9.

Surface quenching techniques are advantageous because the exciton diffusion length is directly measured. As discussed later, most other techniques first fit for the diffusion coefficient which is then used to determine the diffusion length. However, knowledge is the

diffusion coefficient is also useful for the study of exciton dynamics. The diffusion coefficient can be determined from surface quenching techniques if the exciton lifetime, τ, of the pristine PL decay is measured. For the time-integrated case, the information of PL can be used to determine the exciton lifetime τ. We first integrate out x over (0, d) in Equation 3 with boundary conditions for the nonquenching case and get

$$\frac{dn(t)}{dt} = -\frac{n(t)}{\tau} + G(t), \tag{10}$$

where $n(t) = \int_0^d n(x,t)dx$ with initial condition $n(t=0) = 0$, and $G(t) = \int_0^d G(x,t)dx$ which is still a delta-type function. If $0 \le t < t_0$, then $n(t) = 0$. When $t > t_0$, $\frac{dn(t)}{dt} = -\frac{n(t)}{\tau}$ with solution $n(t) = n(t_0)e^{-\frac{t-t_0}{\tau}}$, whose decay rate is $-\frac{1}{\tau}$. The diffusion constant is then computed by $D = \frac{L_D^2}{\tau}$.

2. Exciton-Exciton Annihilation

Measurements of exciton diffusion can be done by studying exciton-exciton annihilation (EEA). At high enough excitation densities a pair of excitons can interact with each other and annihilate within their lifetime. This process leads to a loss of excitons at a rate which depends on the excitation intensity and the diffusivity of the excitons. The EEA technique is advantageous because a secondary quencher material is not needed which greatly simplifies fabrication and modeling. The EEA technique assumes efficient exciton-exciton annihilation. This technique also approximates the annihilation radius from the density as discussed later.

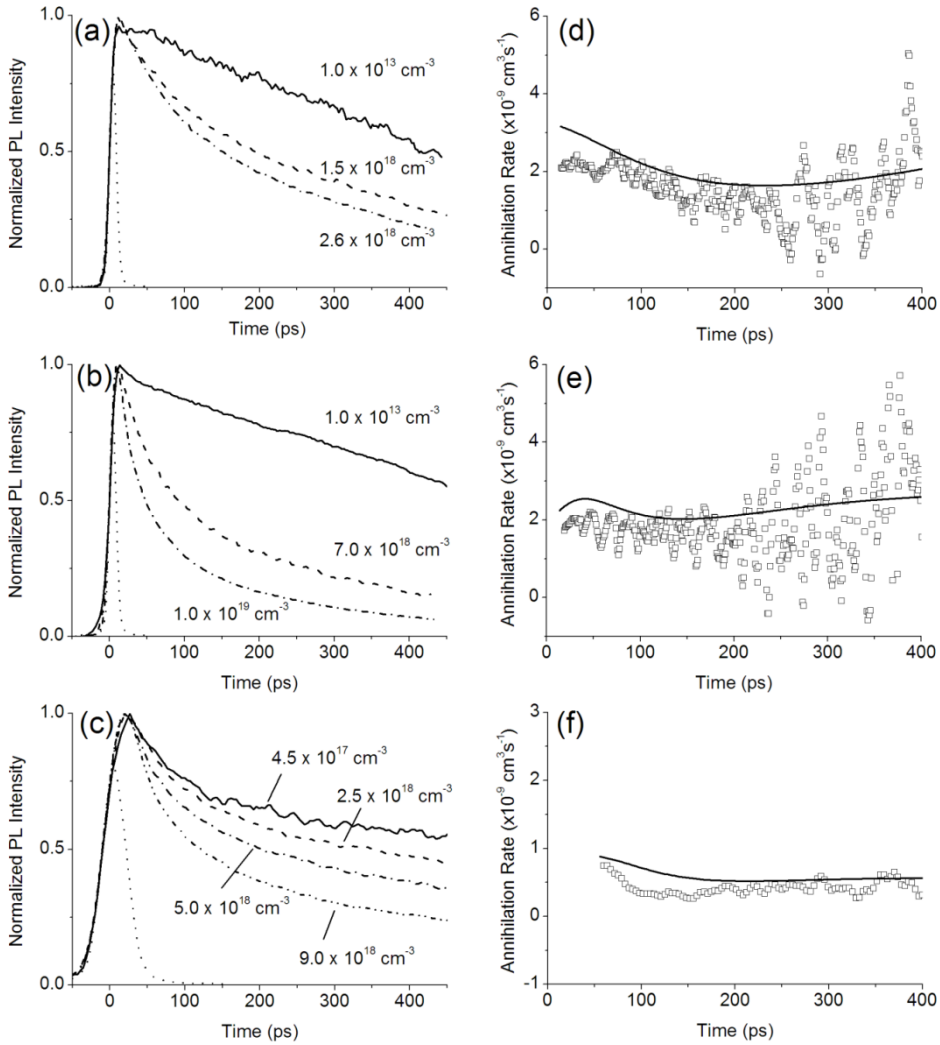

Fig. S5 Photoluminescence decays at different excitation densities and time dependence of the annihilation rate measured in films of A (a,d), B (b,e) and C (c,f). Dotted lines on the left panel are the instrument response functions (IRF) for the decays shown. Solid lines on the right panel are the annihilation rates obtained from the deconvoluted fits to the PL decays. Apparent oscillations of annihilation rate at early time are a result of smoothing which was applied to PL kinetics before their differentiation.

The sample fabrication procedure involved first making solutions in chloroform and stirring them overnight at 50°C. Films were then spin-coated on fused silica substrates which had previously been cleaned via ultra-sonication with acetone and isopropanol for 15

minutes each followed by drying with a N_2 gun. A 1 mL syringe was used with a 0.1 µm PTFE filter to spin-coat the films. Spin-coating was done in the nitrogen glovebox using spin speeds of 1500 – 2000 rpm for duration of 60 seconds typically. No heat treatment was performed on these films and measurements performed on the same day the films were spin-coated. Film samples were transferred to the sample chamber and sealed within the glovebox.

Exciton-exciton annihilation measurements were performed using 100 fs laser pulses at a repetition rate of 5 kHz for excitation and a Hamamatsu C6860 synchroscan streak camera for detection. Samples were kept in the nitrogen atmosphere during measurements. The energy of the laser pulses was controlled with neutral density filters. The excitation spot was measured with a LaserCam 3D beam profiler and found to be an ellipse with the major and minor diameters of 290 µm and 215 µm. Measurements using different excitation wavelengths (400 nm and 570 nm) gave very similar annihilation rates. PL decays at low excitation density were measured using 100 fs pulses at 400 nm with the 80 MHz repetition rate. Figure S5 shows the intensity-dependence of time-resolved fluorescence of compound A, B, and C.

Film thicknesses were estimated using ellipsometry measurements. Spectroscopic ellipsometry measurements were performed in air over a wavelength region 190-1700 nm with a J. A. Woollam Co. Inc. M-2000DI ellipsometer. Normal incidence was used for transmission measurements whereas for reflection measurements the incidence angle was varied between 15º and 45º to the normal. To model the optical constants n (refractive index) and κ (extinction coefficient) and the thickness d, an isotropic optical model was assumed. The optical constants were first modeled in the transparent region above 750 nm where $\kappa = 0$ and was fitted using the Cauchy equation. The data in the transparent region was then fitted to solely in terms of the refractive index and the thickness to give a unique solution. To obtain the optical constants for the full spectral range, the film thickness was fixed and n and κ were selected as fitting parameters. Backside reflections were supressed by applying scotch tape to the back of substrates.

In order to extract quantitative parameters from the measured fluorescence decays (Fig. S5), the following analysis is used. In the absence of exciton-exciton annihilation the exciton density N_1 which is proportional to the time-resolved PL intensity can be described by a rate equation

$$\frac{dN_1}{dt} = -kN_1 \tag{11}$$

where k is a linear decay rate. When annihilation is present, the exciton density N_2 is described by

$$\frac{dN_2}{dt} = -kN_2 - \gamma {N_2}^2 \tag{12}$$

where γ is the annihilation rate. By combining Equation 11 and Equation 12 we get

$$\gamma = \frac{1}{N_2}\left\{\frac{dN_1/dt}{N_1} - \frac{dN_2/dt}{N_2}\right\} \tag{13}$$

This approach to data analysis is similar to the one described by Gulbinas et al[21] except that we use the fluorescence decay at a very low excitation density as a reference. Figure S5d-f shows γ calculated using Equation 13 which was averaged over several decays with different excitation densities. The PL decay at low intensity was fitted with a bi-exponential decay function to reduce the noise and smoothing was applied to differentiation of the PL decays at high intensities. We also used deconvoluted fits to a 3-exponential decay function to calculate γ. The deconvoluted fits give more accurate representation of the fast decays at high intensity and provide more precise scaling of the PL intensity with exciton density, therefore we consider γ values from the deconvoluted fits more accurate. We observe a decrease of the γ value from its initial value in the first 100 ps in all three materials. Time-dependent γ can be observed due to several causes. One possible cause is very slow exciton diffusion, in that case exciton-exciton annihilation could only occur by direct Förster energy transfer onto an excited chromophore which is called static annihilation.[22] Another possible cause is exciton diffusion being restricted to one dimension. In a simplified picture, time-dependence in both static annihilation and restricted diffusion can be explained by fast annihilation of the nearest distance excitons and much slower annihilation of excitons which are further apart. In both cases, it would show $\gamma(t) = \gamma_0/\sqrt{t}$ dependence.[21–23,11,24] We can discount both these processes because the time dependence in Fig. S5 is much weaker than $\gamma_0/\sqrt{t}$ dependence. We explain it by time dependence of exciton diffusion which in disordered materials is expected to slow down with time because the spectral overlap between fluorescence and absorption reduces as excitons progressively populate lower energy sites until a thermal equilibrium is reached. On a time scale t > 100 ps the time-independent annihilation rate is observed. A similar behaviour has been observed in earlier studies of singlet[21–23,11,24–26] or triplet exciton[27,28] diffusion in organic semiconductors. In order to estimate the diffusion coefficient D in thermal equilibrium we use γ values at t>100 ps and the Smoluchowski equation

$$\gamma(t) = 4\pi R_a D\left(1 + \frac{R_a}{\sqrt{2\pi Dt}}\right) \tag{14}$$

where R_a is the annihilation radius. The time-dependent term is negligible after 5 ps. Equation (14) is strictly valid only for isotropic exciton diffusion and isotropic exciton-exciton interactions. We find that films A, B, and C are predominantly isotropic (See Section 8). In semi-crystalline materials both can be anisotropic, however, in case of preferentially one-dimensional diffusion and interaction the annihilation rate has a similar expression to Equation (14) but D in this case is an effective diffusion coefficient.[29] We assume that dissociation of higher energy excitons into electron-hole pairs is negligible because we do not see any additional fluorescence quenching by generated charges and also because measurements using different excitation wavelengths (400 nm and 570 nm) gave very similar annihilation rates (charge generation yield would be higher at shorter excitation wavelength). The annihilation radius is difficult to determine experimentally. For our calculation of the diffusion coefficients we used the average intermolecular spacing as the R_a value assuming that molecules are positioned in a simple cubic lattice. The results are shown in Table S2 including a one-dimensional diffusion length which is calculated using $L_D = \sqrt{D\tau}$ where τ is the fluorescence lifetime which in case of non-exponential decay is taken as the

weighted average of time constants and pre-exponential factors obtained from the bi-exponential fit.

Table S2 Material properties of pristine films of compounds A, B and C with experimentally measured values of fluorescence lifetimes τ and annihilation rates γ and calculated values of the diffusion coefficients *D* and one-dimensional exciton diffusion lengths L_{1D}.

Material	ρ [gcm^{-3}]	*Ra* [nm]	γ [$\times 10^{-9}$ cm^{3}s^{-1}]	*D* [$\times 10^{-3}$ cm^{2}s^{-1}]	τ [ps]	L_{1D} [nm]
A	1.175	1.0	1.9 ± 0.6	1.5 ± 0.4	1450 ± 100	14.5 ± 2.2
B	1.221	1.1	2.1 ± 0.6	1.5 ± 0.4	1370 ± 20	14.5 ± 2.2
C	1.234	1.1	0.6 ± 0.2	0.4 ± 0.1	1620 ± 20	8.4 ± 1.3

Relative to other techniques, the EEA method yielded a greater exciton diffusion coefficient for compounds A and B but a similar value for compound C. As shown in Figure 3, molecular ordering in films of compounds A and B is greater than in films of compound C. This observation suggests that the efficiency of the exciton-exciton annihilation is higher in more ordered materials. This can be explained by the fact that excitons diffuse from amorphous to crystalline regions where they have lower energy. Exciton-exciton annihilation is therefore more likely to occur in crystalline regions where exciton diffusion is enhanced. In other bulk quenching techniques – such as BQ-MC and BQ-SV – exciton quenching is probed in both amorphous and crystalline region which may explain the lower diffusion coefficients relative to EEA. From this, it is expected that amorphous compounds such as compound C would yield similar diffusion coefficients for EEA and other bulk quenching techniques. Indeed, EEA and other bulk quenching methods yielded a similar diffusion coefficient around 0.4×10^{-3} cm^2/s for compound C.

3. Time Resolved Photoluminescence Bulk Quenching Analysed with Monte Carlo Simulation Software (BQ-MC)

The challenge when employing the SS-SQ and TR-SQ techniques is the non-trivial fabrication of bilayer films which have a sharp interface and a high quenching efficiency. An alternative technique which does not require bilayer films is time-resolved PL bulk quenching modeled with a Monte Carlo simulation (BQ-MC). Film fabrication for the BQ-MC technique is relatively simple as it involves spin coating blend solutions of the organic semiconductor with increasingly greater concentrations of PCBM. The BQ-MC technique can be performed with as little as eight films. BQ-MC probes the micromorphology of the blend to make sure that PCBM mixes homogeneously with the organic semiconductor. As will be shown later, PCBM may tend to cluster at higher concentrations. BQ-MC is described in detail in [Mikhnenko Enegy & Env. Sci.] and the simulation is available for free at http://mikhnenko.com/eDiffusion.[30]

In regards to film fabrication, all solutions were stirred and heated overnight at 60 °C. Films were prepared by spin casting at 700 rpm for 60 seconds onto 3 cm × 3 cm (Corning) substrates in a glove box. Blend solutions were prepared by subsequent additions of the 1 mg/mL PCBM to the 5 mg/mL organic semiconductor solution. To prevent photodegradation, all films were encapsulated in an equivalent manner as discussed in the SS-SQ and TR-SQ section above.

PL measurements were performed by exciting samples at 380 nm with frequency doubled 100 fs laser pulses from a Ti-sapphire laser. Time-resolved PL was measured with a Hamamatsu streak camera. Measured decay curves were normalized by the value at time zero and fitted to a single exponential decay. Fitted decay curves were integrated in order to calculate the quenching efficiency Q:

$$Q = 1 - \frac{\int PL_{blend}\, dt}{\int PL_{pristine}\, dt} \tag{15}$$

where $\int PL_{blend} dt$ and $\int PL_{pristine} dt$ are the integrated time-resolved PL for the blend and pristine organic semiconductor films respectively. The PL decays were normalized to the value at t=0 prior to the integration. Figure S6 shows the time-resolved PL for A (Fig. S6a), B (Fig. S6b), and C (Fig. S6c) blended with varying concentrations of PCBM. The PL decay rate increases for greater PCBM volume fractions. Using Equation 15, the relative quenching efficiency was calculated for blend films as shown in Figure S7. To determine the exciton lifetime, the PL decay curves for the pristine films were fitted to a single exponential decay. Pristine films lifetimes are summarized in Table S1.

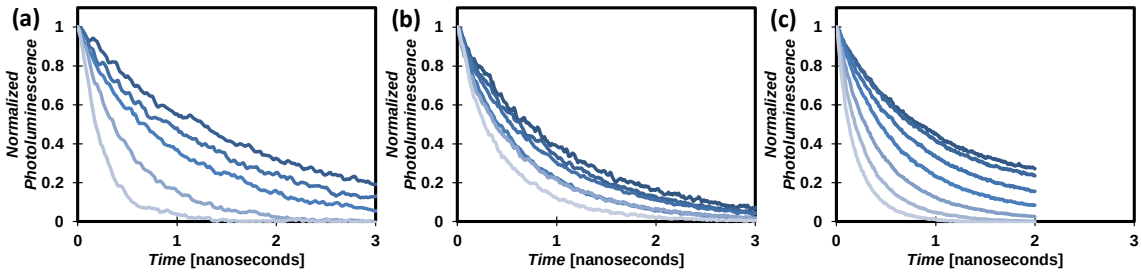

Fig. S6 Time-resolved PL for blend films of (a) A, (b) B, and (c) C with a C_{60} (4 nm) quenching layer for decreasing thickness (dark to lighter curves). All decay curves were normalized by the value at time zero.

Analysis with the BQ-MC technique involves inputting the pristine film lifetime and experimentally measured quenching efficiencies into a Monte Carlos simulation[30] which fits for the diffusion coefficient. In Figure S7, the experimentally measured relative quenching efficiencies (open circles) are fitted (red line) with the Monte Carlo simulation. At high PCBM volume fractions the experimentally measured relative quenching efficiencies for A, B, and C begin to taper off from the simulated curve. This has been observed in other systems[30,31] and is likely due to clustering of PCBM molecules at higher concentrations which reduces the effective quenching volume and therefore the total quenching efficiency. This effect can also arise when the lifetime of excitons in the films approaches the

instrument response function (IRF) which would artificially extend the measured lifetime thereby reducing the quenching efficiency.

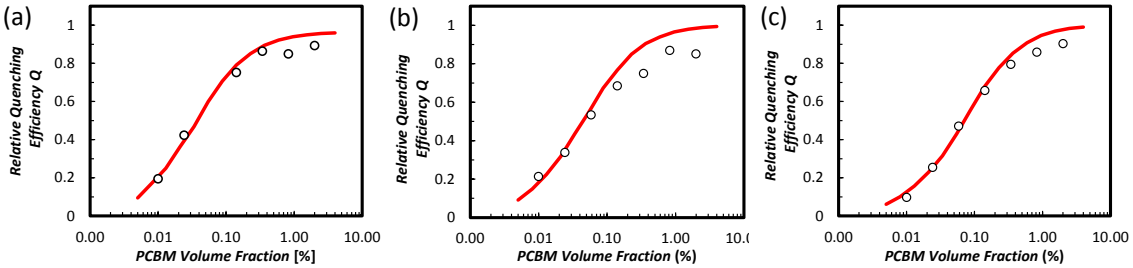

Fig. S7 Time-resolved PL quenching on blend films. Relative quenching efficiency as a function of PCBM volume fraction for (a) A, (b) B, and (c) C blends. Measured data (black dots) were simulated (red line) with a Monte Carlo program.

4. Time-Resolved Photoluminescence Bulk Quenching Analysed with Stern-Volmer Equation (BQ-SV)

For materials that exhibit mono-exponential decay, the Stern-Volmer analysis can be applied instead of Monte Carlo simulation. The advantage of the BQ-SV technique is that modeling software is not needed since the diffusion coefficient determined by a simple fit to the Stern-Volmer equation. The BQ-SV technique assumes single exponential decay and a 1 nm center to center distance for the exciton and organic semiconductor.

In the BQ-SV technique, the measured PL decay from pristine and blend films are fitted to a single exponential to obtain the lifetime for the pristine and blend films. The fitted lifetimes are then used to plot inverse lifetime versus PCBM concentration which is then fitted with the Stern-Volmer equation:[32]

$$\frac{1}{\tau} = \frac{1}{\tau_f} + 4\pi r D c, \tag{16}$$

where τ_f is the lifetime of the pristine film, τ is the lifetime of the blend film, r is the sum of the exciton and PCBM radii, D is the diffusion coefficient, and c is the concentration of PCBM. The r value is the center to center distance between the exciton and PCBM which is approximated at 1 nm. The exciton diffusion length is obtained by inputting the fitted diffusion coefficient and the pristine film lifetime into Equation 16.

Knupfer et al. showed that the gap exciton extension or exciton size scales linearly with the molecular size for π-conjugated molecules.[33] In general, the exciton size was found to be roughly 0.5 nm smaller than the molecular size. For compounds A, B, and C the conjugated backbone is roughly 2-2.7 nm. Following the trends observed by Knupfer et al., we expect an exciton size of 1.5-1.7 nm and a radius of 0.75- 0.88 nm. Given that the PCBM radius is roughly 0.5 nm, the center to center distance, r, between the exciton and PCBM is roughly 1.25-1.33nm. It should be noted a r between 1.25-1.33 nm is an upper limit since it is the center to center distance when the conjugated backbone is normal to the PCBM sphere. A lower r is expected when the conjugated backbone and PCBM are face-on. We therefore believe that 1 nm is a reasonable approximation for r.

In Figure S8, the inverse lifetimes for A (black circles), B (red squares), and C (blue triangle) blend films are plotted against PCBM concentration and subsequently fitted for the diffusion coefficient using Equation 16 in the linear regime. Figure S8 shows that the Stern-Volmer equation fits well at the low PCBM concentration but deviates at PCBM concentrations above 60 × 10^{17} m^{-3}. The observed deviations are likely due to the inability to form a homogenous distribution of PCBM molecules at higher concentrations. The diffusion coefficient and exciton diffusion length obtained with the BQ-SV technique is summarized in Table 1 and Figure 2.

The BQ-SV technique is useful when access to simulation software is not possible. It should be noted here that this technique is only valid for monoexponential decay. In contrast, the BQ-MC technique can be performed with first, second, or third order exponential decay which makes the BQ-MC technique applicable to a larger set of materials.

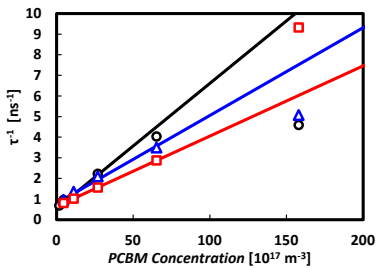

Fig. S8 Time-resolved PL quenching on blend films. Inverse lifetime as a function of PCBM concentration for A (black circles), B (red squares), and C (blue triangles) blends. Measured data (markers) were fitted (lines) Stern-Volmer equation.

5. Exciton diffusion length from FRET theory

Exciton diffusion in π-conjugated polymers occurs via a hopping mechanism mediated by Förster resonant energy transfer (FRET). The exciton diffusion coefficient can thus be calculated from the spectral overlap of absorption and emission of the chromophores. In this

technique the largest deviation arises from the approximation of the intermolecular distance as will be discussed later.

According to the Einstein-Smoluchowski theory of random walks, the diffusion coefficient in a 3D system can be expressed as[34]

$$D = \frac{R^2}{6\tau_{hop}}, \tag{17}$$

where R is the inter-chromophore distance, and τ_{hop} is the exciton hopping time. From FRET theory

$$\tau_{hop} = \tau\left(\frac{R}{R_0}\right)^6, \tag{18}$$

where τ is the fluorescence lifetime in film and R_0 is the Förster radius which was calculated from the extinction coefficient and PL spectra shown in Figure S9 below. For our calculations, the closest intermolecular distance estimated from Kim et al[16] is taken as the inter-chromophore distance R.

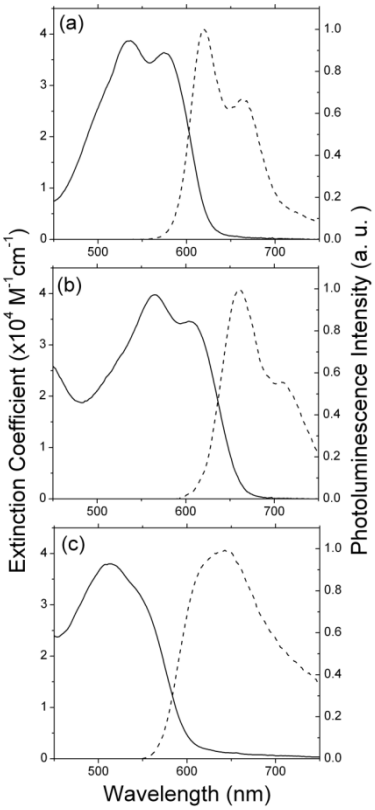

Fig. S9 Molar extinction coefficient obtained using spectral ellipsometry and normalized PL spectra of films spin-coated on fused silica substrates for compounds (a) A, (b) B and (c) C.

The Förster radius R_0 is calculated from the spectral overlap using:

$$R_0^6 = \frac{9000(\ln 10)k^2 Q_Y}{128\pi^5 N_A n^4}\int_0^\infty F(\lambda)\varepsilon(\lambda)\lambda^4 d\lambda, \tag{19}$$

where k^2 is the relative orientation of dipoles (k^2 = 0.476 assuming rigid and randomly oriented dipoles), Q_y is the PLQY in film, n is the average refractive index of the medium in the wavelength range at which spectral overlap is significant, $F(\lambda)$ is the corrected fluorescence intensity of the film with area normalized to unity and $\varepsilon(\lambda)$ is the molar extinction coefficient in film that was obtained using spectral ellipsometry as described below. It should be noted that a number of works have incorrectly used a k^2 = 2/3. A k^2 = 2/3 is derived from energy transfer that occurs after the donor and acceptor molecules go through randomized rotation diffusion.[32] This is unlikely the case for solid state films which have rigid and randomly oriented dipoles. For rigid and randomly oriented dipoles a k^2 = 0.476 is more appropriate.[35]

Molar extinction coefficient (in $M^{-1}cm^{-1}$) is given by

$$\varepsilon = \frac{A}{cl}, \tag{20}$$

where A is the absorbance, l is the optical path length and c is the molar chromophore concentration, which is

$$c = 1000\frac{\rho}{M_c}, \tag{21}$$

where ρ is the density of the single crystal obtained previously[16] and M_c is the molecular weight of a chromophore. Absorbance is

related to the absorption coefficient α via $A = \alpha l \log_{10} e$ whereby the absorption coefficient is related to the optical constant κ (imaginary part of the refractive index) via $\alpha = \frac{4\pi\kappa}{\lambda}$.

These molar extinction coefficients obtained agree well with published values for these materials in solution.[16] To calculate the diffusion coefficients, an intermolecular distance *R* is assumed. Here, we used the shortest intermolecular distances obtained from x-ray diffraction studies[16] of single crystals to calculate the upper limit of the diffusion coefficient. The lower limit of the diffusion coefficient is estimated by using the average intermolecular distances assuming they are positioned in a simple cubic lattice. This gives a range of values of the diffusion coefficients from a single crystal approximation to an average intermolecular spacing. Table S3 below shows the main values used to calculate the upper and lower limits of diffusion coefficient using these FRET calculations.

Table S3 Calculating upper and lower limits of diffusion coefficients using FRET

Material	PLQY	τ [ns]	Refractive index, *n*	R_0 [nm]	*R* [nm]		*D* [$\times 10^{-3}$ $cm^2 s^{-1}$]		
					Min.	Max.	Min.	Max.	Avg.
A	0.48	1.45	2.32	2.80	0.74	1.04	0.48	2.6	1.53
B	0.14	1.37	2.23	2.35	0.71	1.09	0.15	1.1	0.64
C	0.28	1.62	2.23	2.32	0.91	1.11	0.11	0.33	0.22

The film PLQY were all measured in air and the decay lifetimes were measured under nitrogen. Film PLQY's were typically measured not long after performing annihilation measurements and were exposed to air for less than a few minutes before running the PLQY measurement.

Ellipsometry measurements (as described in Section 2) were performed on these films which allowed the refractive indices to be obtained by modelling of the optical constants as shown in Figure S10.

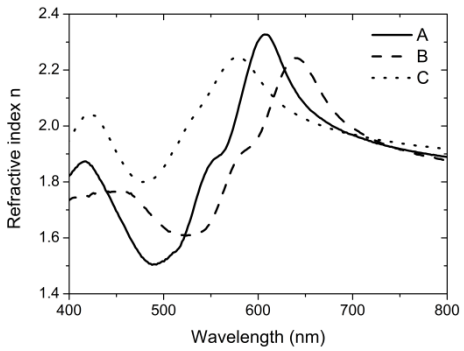

Fig. S10 Refractive indices in the visible region obtained from ellipsometry

6. Measurement of anisotropy and relative crystallinity with X-ray Diffraction

Using a Rigaku Smartlab High-Resolution X-ray Diffractometer, the scattering for the out of plane direction was probed by performing a θ-2θ scan from 2-30^0 with 1.5418 Å CuKα radiation at 40 kV operating voltage and 44 mA operating current. Figure S11 shows the out of plane scattering for films of A, B, and C. Films of A and B exhibited a scattering peak at q_z 1.3 and 1.1 nm^{-1} respectively. Using X-ray diffraction from single crystals, the scattering peaks at q_z values of 1.3 and 1.1 nm^{-1} for films A and B are indexed as the (100) plane. No scattering was detected in films of C (dashed green line in Fig. S11). In order to quantitatively compare A and B the measured scattering intensity must be corrected for crystallites texturing, thickness, reflection structure factor and multiplicity, unit cell volume, and the Lorenz-Polarization factor.

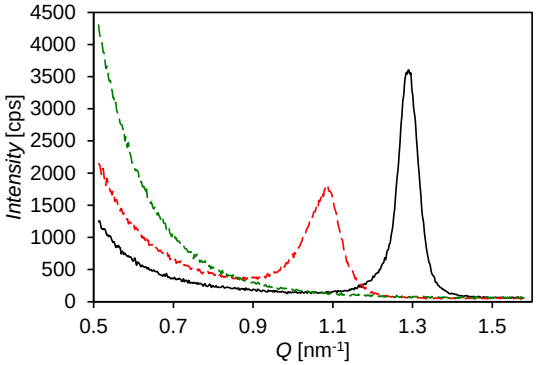

Fig. S11: Out of plane X-ray diffraction scattering of films A (solid black line), B (dashed red line), and C (dashed green line).

To probe crystallite texturing in films of A and B a pole figure was created by measuring the scattering intensity form the (100) plane of A and B as a function of Chi (the polar angle).This was done by fixing q_z at 1.3 (1.1) nm^{-1} and scanning from Chi values of -5^0 to 90^0 (Fig. S12). Figure S12 shows that films of A and B exhibit a strong peak intensity at Chi = 0˚. This result indicates that crystallites in films of A and B are preferentially oriented with the (100) plane parallel to the substrate and textured in the out of plane direction.

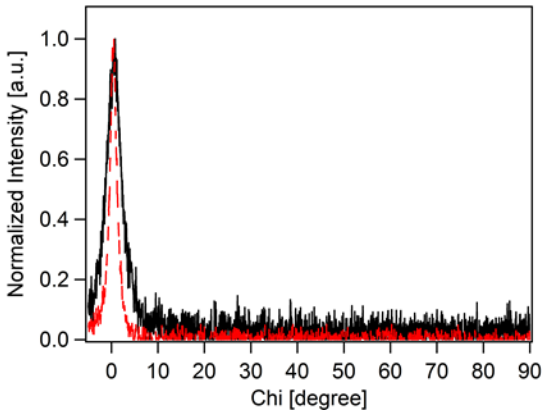

Fig. S12: Pole figure for films of A (black line) and B (red dashed line). The scattering intensity was collected at 4.8 and 5.6 2θ for films of A and B respectively which corresponds to the diffraction from the (100) plane.

Since the crystallites in films A and B are predominantly textured in the out of plane direction, it is possible to determine the relative crystallinity of films A and B with proper normalization of the out of plane scattering observed in Figure S11. Figure 3 shows the out of plane scattering for films A and B which has been normalized by the thickness, structure factor, multiplicity, unit cell volume, and the Lorenz-Polarization factor (Table S4).[36] The structure factor, multiplicity and unit cell volume were obtained from the single crystal structures.[16] The integrated scattering intensity from A is roughly 1.6 times greater than B. This result indicates that films of A have a greater volume of crystalline material relative to films of B. In summary, we find that the relative crystallinity follows A > B > C. It is important to note that X-ray diffraction experiments do not tell what percentage of film volume is crystalline as compared to amorphous volume.

Table S4 Normalization Parameters for X-Ray Diffraction

	A	B	C
Thickness (nm)	106	113	83
Structure Factor	140.91	172.19	209.91
Multiplicity	2	2	2
Unit Cell Volume ($Å^3$)	2229.9	2563.6	5431.8

7. Measuring anisotropy in bulk film with spectroscopic ellipsometry

Anisotropy can impact the directionality and efficiency of exciton diffusion. It can also result in a difference in exciton diffusion length for techniques which measure exciton diffusion length normal to the substrate in comparison to techniques which measure exciton diffusion in 3D. For this reason, it is important to investigate the degree of anisotropy in films of A, B, and C. Figure S10 showed that crystallites in films A and B are highly textured out of plane and therefore anisotropic. While our x-ray diffraction measurements confirm the presence of anisotropy, it does not quantify degree of anisotropy since the volume fraction of amorphous and crystalline regions is not known. It would be ideal to probe the bulk film anisotropy. A number of studies have shown that spectroscopic ellipsometry is a useful technique to measure bulk film anisotropy since both amorphous and crystalline regions are probed.[37–39] Spectroscopic ellipsometry can be used to model the magnitude of absorption for both the in and out of plane directions. For a highly anisotropic film, molecules and their transition dipoles are preferentially oriented in a specific direction. This preferential orientation induces a difference in absorption for the

in and out of plane directions which is correlated to the degree of anisotropy.

.

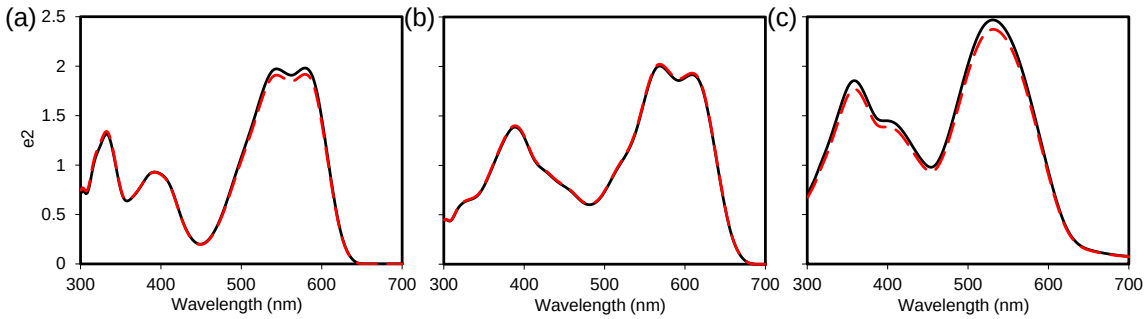

Fig. S13: Modeled $e2_{in\text{-}plane}$ (black line) and $e2_{out\text{-}plane}$ (dashed red line) for films of (a) A, (b) B, and (c) C.

It is useful to first discuss the expected in and out of plane absorption of our films if they were highly crystalline and anisotropic. Figure S12 showed that crystallites in films of A and B are preferentially oriented with the (100) plane parallel to the substrate. When the (100) plane is parallel to the substrate, molecules of A and B have their conjugated backbone nearly parallel to the substrate as determined form the single crystal structures.[16] Density function theory calculations showed that the transition dipole lies along the conjugated backbone for molecules A, B, and C. It is therefore expected that a highly anisotropic film of A or B would strongly absorb electrical fields which are also parallel to the substrate. Since the electrical field is perpendicular to the direction of the propagation vector, we would expect a strong absorption for light incident perpendicular to the substrate. The magnitude of absorption can be quantified by modeling the extinction coefficient, *k*, or the imaginary component of the dialectic constant, *e2*. By convention, a subscript is added to identify the direction of the electrical field that gives rise to the absorption. Previous works have denoted absorption from electrical fields parallel to the substrate as $e2_{in\text{-}plane}$, $e2_x$, or $e2_{ordinary}$.[37–39] Likewise, absorption from electrical field perpendicular to the substrate has been referred to as $e2_{out\text{-}plane}$, $e2_z$, or $e2_{extraordinary}$. If films of A(B) are highly anisotropic, then we would expect the magnitude of $e2_{in\text{-}plane}$ to be significantly greater than that of $e2_{out\text{-}plane}$.

To probe anisotropy, films of A, B, and C where prepared at three different thicknesses spanning 20-100 nm by varying the concentration. All films where spin casted from chloroform at 2000 rpm for 60 seconds. Spectroscopic ellipsometry was measured on films of A, B, and C as described in Section 2. Additionally, the thickness and RMS roughness where measured with profilometer and atomic force microscopy in order to reduce the number of fit parameters in optical modeling. Multiple quartz substrates where initially modeled with a Cauchy model to determine the substrate optical constants. Optical constants for A, B, and C were fit with a B-Spline model[40] and the anisotropy type set to Biaxial. Kramers-Kronig Mode, Difference Mode, and force *e2* positive was turned on for fitting. Fit parameters included the in and out of plane dielectric constant along with the anisotropy parameter dZ_A. Fitting was done with individual samples along with multi-sample analysis. Similar results were obtained for individual and multi-sample analysis. Figure S13 shows *e2* obtained from the multisampling fits of films A, B, and C. For all three compounds, $e2_{in\text{-}plane}$ is only slightly greater than $e2_{out\text{-}plane}$. As discussed above, we would expect $e2_{in\text{-}plane}$ to be significantly greater than $e2_{out\text{-}plane}$ if films of A and B were highly anisotropic. The similar magnitudes of $e2_{in\text{-}plane}$ and $e2_{out\text{-}plane}$ suggest that the majority of molecules in films of A, B, and C have isotropic orientation. Interestingly, our x-ray diffraction studies showed that there exist crystallites in films of A and B with anisotropic orientation. It is likely that the volume fraction of anisotropic crystal is small due to the fact that all films where prepared from a low boiling point solvent and a relatively high spin speed, which would promote the formation of isotropic films.

References

1. M. Theander, A. Yartsev, D. Zigmantas, V. Sundström, W. Mammo, M. R. Andersson, and O. Inganäs, *Phys. Rev. B*, 2000, **61**, 12957.
2. D. E. Markov, C. Tanase, P. W. M. Blom, and J. Wildeman, *Phys. Rev. B*, 2005, **72**, 045217.
3. D. E. Markov, E. Amsterdam, P. W. M. Blom, A. B. Sieval, and J. C. Hummelen, *J. Phys. Chem. A*, 2005, **109**, 5266–5274.
4. Y. Wu, Y. C. Zhou, H. R. Wu, Y. Q. Zhan, J. Zhou, S. T. Zhang, J. M. Zhao, Z. J. Wang, X. M. Ding, and X. Y. Hou, *Appl. Phys. Lett.*, 2005, **87**, 044104–044104–3.
5. S. R. Scully and M. D. McGehee, *J. Appl. Phys.*, 2006, **100**, 034907.
6. Y. C. Zhou, Y. Wu, L. L. Ma, J. Zhou, X. M. Ding, and X. Y. Hou, *J. Appl. Phys.*, 2006, **100**, 023712–023712–5.
7. C. Goh, S. R. Scully, and M. D. McGehee, *J. Appl. Phys.*, 2007, **101**, 114503.
8. S.-B. Rim, R. F. Fink, J. C. Schöneboom, P. Erk, and P. Peumans, *Appl. Phys. Lett.*, 2007, **91**, 173504–173504–3.
9. Y. Terao, H. Sasabe, and C. Adachi, *Appl. Phys. Lett.*, 2007, **90**, 103515–103515–3.
10. O. V. Mikhnenko, F. Cordella, A. B. Sieval, J. C. Hummelen, P. W. M. Blom, and M. A. Loi, *J. Phys. Chem. B*, 2008, **112**, 11601–11604.
11. P. E. Shaw, A. Ruseckas, and I. D. W. Samuel, *Adv. Mater.*, 2008, **20**, 3516–3520.
12. S. A. Jenekhe and S. Yi, *Appl. Phys. Lett.*, 2000, **77**, 2635–2637.
13. A. . Manoj and K. . Narayan, *Opt. Mater.*, 2003, **21**, 417–420.
14. M. M. Alam and S. A. Jenekhe, *Chem Mater*, 2004, **16**, 4647–4656.
15. D. J. Lipomi, R. C. Chiechi, W. F. Reus, G. M. Whitesides, D. J. Lipomi, R. C. Chiechi, W. F. Reus, and G. M. Whitesides, *Adv. Funct. Mater. Adv. Funct. Mater.*, 2008, **18, 18**, 3469, 3469–3477, 3477.
16. C. Kim, J. Liu, J. Lin, A. B. Tamayo, B. Walker, G. Wu, and T.-Q. Nguyen, *Chem Mater*, 2012, **24**, 1699–1709.
17. W. Becker, *Advanced Time-Correlated Single Photon Counting Techniques*, Springer, 2005th edn., 2005.

18. G. F. Burkhard, E. T. Hoke, and M. D. McGehee, *Adv. Mater.*, 2010, **22**, 3293–3297.
19. P. Peumans, A. Yakimov, and S. R. Forrest, *J. Appl. Phys.*, 2003, **93**, 3693.
20. J. Nocedal and S. Wright, *Numerical Optimization*, Springer, 2nd edn., 2006.
21. V. Gulbinas, I. Minevičiūtė, D. Hertel, R. Wellander, A. Yartsev, and V. Sundström, *J. Chem. Phys.*, 2007, **127**, 144907–144907–8.
22. M. A. Stevens, C. Silva, D. M. Russell, and R. H. Friend, *Phys. Rev. B*, 2001, **63**, 165213.
23. A. J. Lewis, A. Ruseckas, O. P. M. Gaudin, G. R. Webster, P. L. Burn, and I. D. W. Samuel, *Org. Electron.*, 2006, **7**, 452–456.
24. P. E. Shaw, A. Ruseckas, J. Peet, G. C. Bazan, and I. D. W. Samuel, *Adv. Funct. Mater.*, 2010, **20**, 155–161.
25. A. Ruseckas, M. Theander, L. Valkunas, M. R. Andersson, O. Inganäs, and V. Sundström, *J. Lumin.*, 1998, **76–77**, 474–477.
26. A. Ruseckas, J. C. Ribierre, P. E. Shaw, S. V. Staton, P. L. Burn, and I. D. W. Samuel, *Appl. Phys. Lett.*, 2009, **95**, 183305–183305–3.
27. J. C. Ribierre, A. Ruseckas, K. Knights, S. V. Staton, N. Cumpstey, P. L. Burn, and I. D. W. Samuel, *Phys. Rev. Lett.*, 2008, **100**, 017402.
28. E. B. Namdas, A. Ruseckas, I. D. W. Samuel, S.-C. Lo, and P. L. Burn, *Appl. Phys. Lett.*, 2005, **86**, 091104–091104–3.
29. Z. Masri, A. Ruseckas, E. V. Emelianova, L. Wang, A. K. Bansal, A. Matheson, H. T. Lemke, M. M. Nielsen, H. Nguyen, O. Coulembier, P. Dubois, D. Beljonne, and I. D. W. Samuel, *Adv. Energy Mater.*, 2013, n/a–n/a.
30. O. V. Mikhnenko, H. Azimi, M. Scharber, M. Morana, P. W. M. Blom, and M. A. Loi, *Energy Environ. Sci.*, 2012, **5**, 6960–6965.
31. O. Mikhnenko, J. Lin, Y. Shu, J. E. Anthony, P. W. M. Blom, T.-Q. Nguyen, and M. A. Loi, *Phys. Chem. Chem. Phys.*, 2012, **14**, 14196–14201.
32. J. R. Lakowicz, *Principles of Fluorescence Spectroscopy*, Springer, 2006.
33. M. Knupfer, J. Fink, E. Zojer, G. Leising, and D. Fichou, *Chem. Phys. Lett.*, 2000, **318**, 585–589.
34. R. R. Lunt, N. C. Giebink, A. A. Belak, J. B. Benziger, and S. R. Forrest, *J. Appl. Phys.*, 2009, **105**, 053711.
35. I. Z. Steinberg, *Annu. Rev. Biochem.*, 1971, **40**, 83–114.
36. B. E. Warren, *X-Ray Diffraction*, Courier Dover Publications, 1990.
37. U. Heinemeyer, A. Hinderhofer, M. I. Alonso, J. O. Ossó, M. Garriga, M. Kytka, A. Gerlach, and F. Schreiber, *Phys. Status Solidi A*, 2008, **205**, 927–930.
38. D. M. DeLongchamp, R. J. Kline, D. A. Fischer, L. J. Richter, and M. F. Toney, *Adv. Mater.*, 2011, **23**, 319–337.
39. C. Schünemann, D. Wynands, K.-J. Eichhorn, M. Stamm, K. Leo, and M. Riede, *J. Phys. Chem. C*, 2013, **117**, 11600–11609.
40. B. Johs and J. S. Hale, *Phys. Status Solidi A*, 2008, **205**, 715–719.